Mode Dependency of Quantum Decoherence Studied via an Aharonov-Bohm Interferometer

Tung-Sheng Lo,[1,2] Yiping Lin,[1] Phillip M. Wu,[3] Dah-Chin Ling,[4] C. C. Chi,[1,5] and Jeng-Chung Chen[1,5,*]
[1]*Department of Physics, National Tsing-Hua University, Hsinchu 30013, Taiwan*
[2]*Institute of Physics, Academia Sinica, Taipei 115, Taiwan*
[3]*Department of Applied Physics and Geballe Laboratory for Advanced Materials, Stanford University, Stanford, California 94305, USA*
[4]*Department of Physics, Tamkang University, Tamsui Dist., New Taipei City 25137, Taiwan*
[5]*Frontier Research Center on Fundamental and Applied Sciences of Matters, National Tsing Hua University, Hsinchu 30013, Taiwan*

(Received 31 August 2015; published 24 February 2016)

We investigate the dependence of decoherence on the mode number M in a multiple-mode Aharonov-Bohm (AB) interferometer. The design of the AB interferometer allows us to precisely determine M by the additivity rule of ballistic conductors; meanwhile, the decoherence rate is simultaneously deduced by the variance of the AB oscillation amplitude. The AB amplitude decreases and fluctuates with depopulating M. Moreover, the normalized amplitude exhibits a maximum at a specific M (~9). Data analysis reveals that the charge-fluctuation-induced dephasing, which depends on the geometry and the charge relaxation resistance of the system, could play an essential role in the decoherence process. Our results suggest that the phase coherence, in principle, can be optimized using a deliberated design and pave one of the ways toward the engineering of quantum coherence.

DOI: 10.1103/PhysRevLett.116.080401

Understanding quantum decoherence mechanisms is one of the central themes in mesoscopic physics [1]. In the view of applications, a comprehensive understanding of the underlying physics of quantum coherence lies on the core for developing a reliable quantum information technology [2,3]. The dephasing process involves scattering events of small energy and momentum transfer, degrading the quantum interference phenomena in electrical transport. The predominant decoherence mechanisms, taking a ballistic interferometer for example, have been attributed to thermal averaging [4] and charge-fluctuation-induced dephasing [5]. Thermal averaging ascribes the loss of phase coherence because of the energy averaging of the transmission probability. Charge-fluctuation-induced dephasing is due to the electron-electron $(e-e)$ interaction between the carriers and the surrounding charges. Theoretically, the interaction-induced decoherence is closely related to the geometry of the system [6,7]. Despite numerous studies, the fundamental aspects of the dephasing sources remain unclear to date. This is primarily because of the fact that the known dephasing processes all lead to the suppression of the interference signal with increasing temperature T in a T-dependent measurement, which is the most general approach to obtaining dephasing information [3,8–12]. Therefore, to gain further insight into the decoherence mechanisms requires the use of an experimental knob besides T to distinguish the effects of the different dephasing sources.

A ballistic quantum wire is characterized by its quantized conductance G with plateaus at $G = G_0 M$, where $G_0 = 2e^2/h$ and M is the mode number, denoting the number of occupied one-dimensional (1D) subbands [13]. To probe the phase coherence, a typical method is to use a quantum interferometer, such as a ring-shaped conductor illustrated in Fig. 1(a), consisting of two parallel quantum wires. The conductance of the interferometer can be described as $G = G_1 + G_2 + \Delta G$, where $G_{1(2)}$ is the conductance of the upper (lower) branch. The interference term ΔG contains the phase information. Under a small perpendicular magnetic field, ΔG catches the Aharonov-Bohm (AB) phase of the carriers and oscillates with a flux period of $\Phi_0 \equiv h/e$ [13]. Decoherence abates the AB amplitude; consequently, the dephasing rate Γ_ϕ can be extracted. In the condition $\Delta G \ll G$, the relation $G \sim G_1 + G_2$, referred to as the additivity rule of conductance in parallel coupled quantum wires, is approximately valid [14]. Thus, it is feasible for a ballistic AB interferometer to provide the phase information and the populated mode numbers at once.

In this work, we aim to investigate the mode dependence of the decoherence to address the aforementioned issues by using an AB interferometer with a pair of side gates for modulating the wire widths. For a ballistic wire, M is directly related to its width W, i.e., $W \propto M$ [13]. Besides, the charge-fluctuation-induced dephasing rate Γ_{e-e} is known to be linear with the charge relaxation resistance R_q, which is inversely proportional to M, i.e., $\Gamma_{e-e} \propto TR_q \propto M^{-1}$ [6,15]. In contrast, the dephasing rate of thermal averaging Γ_{th} is believed to be independent of M [9–12]. We seek to evaluate the effects of different dephasing mechanisms with M. Our results show that the

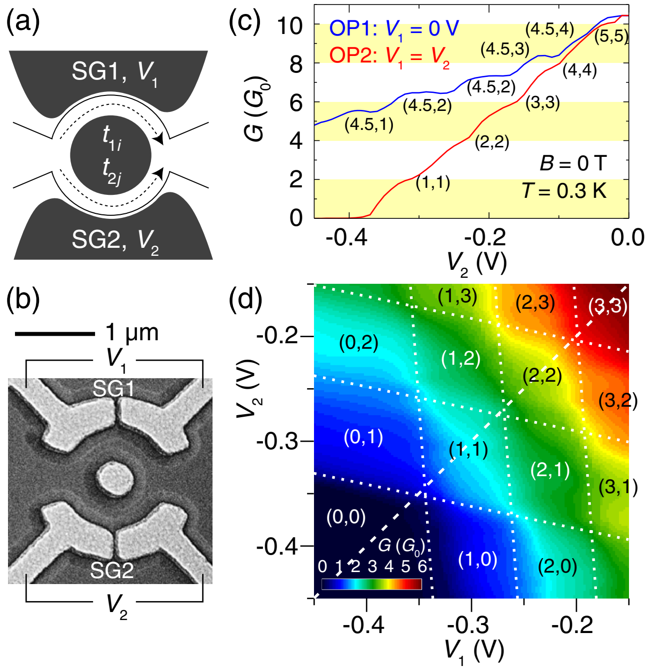

FIG. 1. (a) Schematic diagram of a AB interferometer. The propagating modes residing in the wires can be tuned by applying gate voltages V_1 and V_2 on the side gate SG1 and SG2, respectively. (b) SEM image of the device. (c) Representative conductance traces measured at $T = 0.3$ K. (d) A comprehensive conductance map spanned by V_1 and V_2. The mode numbers in the upper and lower wires are indicated as (M_1, M_2).

interference amplitude per mode reaches an optimized maximum at $M \sim 9$ as a result of a compromise between the two major dephasing effects.

The layout of the interferometers is shown in Fig. 1(a). Figure 1(b) shows the scanning electron microscopy (SEM) image of the devices. The devices were fabricated on modulation-doped GaAs/AlGaAs heterostructures with a two-dimensional electron gas (2DEG) situated 90 nm below the surface. The 2DEG has a carrier density $n_s = 1.8 \times 10^{11}$ cm^{-2} and mobility $\mu = 8.6 \times 10^5$ cm^2/Vs at 4.2 K, corresponding to the mean free path $l_e \sim 6$ μm. The interferometers were defined by wet etching, followed by the deposition of Cr/Au metals for the side gates, SG1 and SG2. The key consideration in designing the devices is to make the junctions at the entrance and exit smoothly connected to the leads and slightly wider than the sum of the widths of the branches, so that the backscattering is reduced—to ensure the additivity rule can hold; meanwhile, the AB phase is still retained [14,16]. The devices were measured in a two-terminal configuration with a 10-μV ac excitation voltage at a frequency of 17 Hz and cooled using a He3 refrigerator with a base temperature of 0.3 K.

The G of the interferometer can be tuned by applying voltages V_1 on SG1 and V_2 on SG2. The interferometer is typically operated in two manners for the AB experiment in this work, termed as operation OP1 and OP2. For OP1, G of one branch alone is modulated by changing V_2 only and keeping $V_1 = 0$ V. As denoted by the blue trace in Fig. 1(c), the stairlike descent in steps of G_0, taken as a sign of the successive depopulation of one mode in the lower wire, is clearly observed. For OP2, G of both branches are simultaneously varied by biasing $V_2 = V_1$. The red trace in Fig. 1(c) shows the stairlike decrease in steps of $2G_0$, suggesting the sequential depletion of one mode in each wire. Figure 1(d) shows the conductance map as a function of V_1 and V_2 [17]. The conductance map is rather symmetric about $V_1 = V_2$ (dashed line). The dotted lines in Fig. 1(d) indicate the border lines between two adjacent plateaus. As only one wire is transmissive, the strip plateaus of quantized conductance in units of G_0 are found. While both wires are transmissive, the diamondlike patches are observed. The resolved $2G_0$ steps in symmetric gate biasing and appearance of the diamondlike patches demonstrate the evidences for the additivity rules [14,18,19].

The conductance map provides a means to determine the mode numbers in the interferometer. $G_{1(2)}$ can be described by the Landauer formula as $G_1 = G_0 \sum_{i=1}^{M_1} |t_{1i}|^2$ ($G_2 = G_0 \sum_{j=1}^{M_2} |t_{2j}|^2$), where $t_{1i(2j)}$ represents the transmission amplitude of the ith (jth) mode in the upper (lower) wire, having an integer number $M_{1(2)}$ of modes resident [see Fig. 1(a)]. Here, we consider generalized $M_{1(2)} = G_{1(2)}/G_0$ and $M = G/G_0$ to account for both fully and partially transmissive channels. Based on the plateau configurations associated with G_1 and G_2, we can identify the mode numbers (M_1, M_2) at a given (V_1, V_2), as marked in Figs. 1(c) and 1(d). We estimate $M_1 \sim 4.5$ and $M_2 \sim 6$ for $V_1 = V_2 = 0$. We checked that the additivity rule approximately holds, implying $M \sim M_1 + M_2$, with an error on the order of 1% of $M_1 + M_2$. The resolved quantized plateaus on G_1 and G_2 allows us not only to ensure that the interferometer is in the ballistic regime but also to determine the exact mode numbers, M_1 and M_2, involved in ΔG. In the following discussion, the aforesaid ΔG contributed by the AB interference is denoted as ΔG_{AB}.

We turn to the investigation of the correlation between decoherence and the mode numbers. Figure 2(a) demonstrates a typical magnetoconductance $G(B)$ trace manifesting the AB oscillations at $V_1 = V_2 = 0$ V. The $G(B)$ trace is nearly symmetric about $B = 0$ T. The frequency of the oscillation is $\Delta B^{-1} = 0.18 \pm 0.08$ mT^{-1}, extracted from the fast Fourier transform (FFT) of $G(B)$ after the subtraction of an aperiodic background, as shown in Fig. 2(b). We only observe the h/e fundamental harmonic, corresponding to a circular path with radius $r = \sqrt{h/e\pi\Delta B} = 474 \pm 111$ nm. The AB oscillation amplitude $|\Delta G_{\mathrm{AB}}|$ is obtained by integrating the h/e FFT peak. Figures 2(c) and 2(d) show the evolution of ΔG_{AB} for OP1 and OP2, respectively. The intensity plot of ΔG_{AB} on the B-V_2 plane reveals how the AB oscillation varies with the mode numbers. With the depopulation of the modes in one or both wires, the

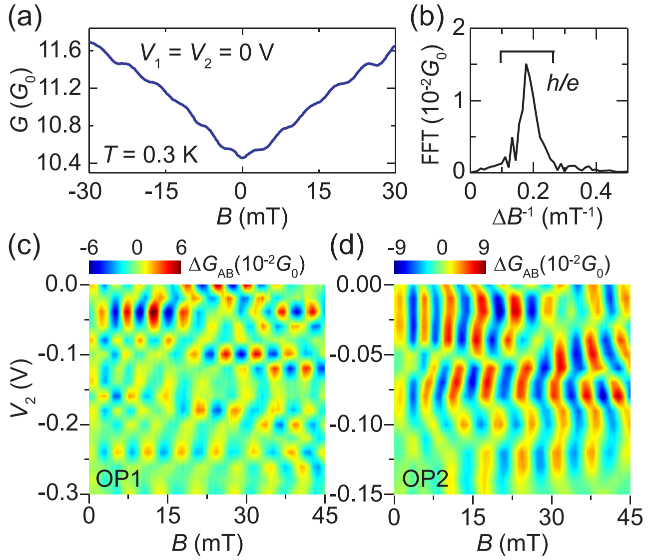

FIG. 2. (a) A representative trace of AB oscillations in the magnetoconductance measured at $V_1 = V_2 = 0$ V and $T = 0.3$ K. (b) Fast Fourier spectrum of the trace in (a) after deducting an aperiodic background. (c) and (d) The evolution of the AB oscillation component ΔG_{AB} as a function of V_2 for operations OP1 and OP2, respectively.

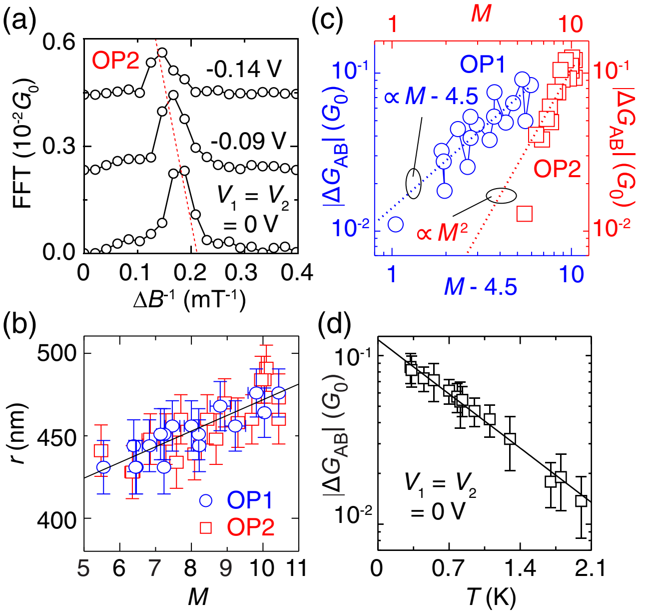

FIG. 3. Data analysis of AB oscillations. (a) Representative FFT spectra of ΔG_{AB} in Fig. 2(d). (b) The radius r as a function of M. (c) $|\Delta G_{\mathrm{AB}}|$ as a function of $M - 4.5$ for OP1 and M for OP2. (d) The temperature dependence of $|\Delta G_{\mathrm{AB}}|$ taken at $V_1 = V_2 = 0$ V.

oscillatory features gradually diminish and exhibit a gradual phase shift and a random π phase jump.

To investigate the decoherence in the multiple-mode interferometer, we can express ΔG_{AB} as [5,6,20,21]

$$\Delta G_{\mathrm{AB}} = 2e^{-\tau\Gamma_\phi} G_0 \sum_{i,j} |t_{1i}||t_{2j}| \cos\left(2\pi\frac{\Phi}{\Phi_0} + \delta_{ij}\right), \qquad (1)$$

where $\tau \equiv L/v_{\mathrm{F}}$ is the electron traversal time through half the circumference $L \equiv \pi r$ with Fermi velocity $v_{\mathrm{F}}(\sim 1.84 \times 10^5\ \mathrm{m/s})$, and δ_{ij} accounts for the phase difference between two paths at $B = 0$ T. While the electron trajectories are pushed toward the inner wall of the ring by a negative gate voltage, the mean radius reduces, and the h/e FFT peak shifts to lower frequency, as demonstrated in Fig. 3(a). In Fig. 3(b), r is plotted vs M and shows a linear relationship $r(M) = 9.5M + 377$ nm. For $M \sim 10.5$ at $V_1 = V_2 = 0$ V, we obtain $r(M) \sim 477$ nm, in agreement with the mean radius evaluated from the SEM image [see Fig. 1(b)].

Figure 3(c) shows the dependence of $|\Delta G_{\mathrm{AB}}|$ on M. We find that $|\Delta G_{\mathrm{AB}}|$ fluctuates and decreases with reducing M. Let us first focus on the general decline trend of $|\Delta G_{\mathrm{AB}}|$. As indicated by the dotted lines in Fig. 3(c), $|\Delta G_{\mathrm{AB}}| \propto M - 4.5$ for OP1 and $|\Delta G_{\mathrm{AB}}| \propto M^2$ for OP2. To understand these distinct dependences, we note that from Eq. (1), $|\Delta G_{\mathrm{AB}}|$ is directly proportional to the term $\sum_{i,j}|t_{1i}||t_{2j}|$, which sums up all accessible modes involved in ΔG_{AB}. The observation of well-resolved plateaus allows us to reasonably assume $|t_{2j}| = 1$ for OP1 and $|t_{1i}| = |t_{2j}| = 1$ for OP2 when counting fully transmissive modes. For OP1, where the upper wire retains a nearly constant value of $M_1 \sim 4.5$ so that $M_2 \sim M - 4.5$, we have $\sum_{i,j}|t_{1i}||t_{2j}| \propto \sum_j |t_{2j}| = M_2 \sim M - 4.5$. In contrast, for OP2, we have $M_1 \sim M_2 \sim M/2$, and the summation is given by $\sum_{i,j}|t_{1i}||t_{2j}| = (\sum_i |t_{1i}|)^2 = M_1^2 \propto \sim M^2$. The observed correlations of $|\Delta G_{\mathrm{AB}}|$ with M can be summarized as the relation $|\Delta G_{\mathrm{AB}}| \propto \sim M_1 M_2$, suggesting that each mode equally contributes to ΔG_{AB}.

We now proceed to discuss the fluctuations in $|\Delta G_{\mathrm{AB}}|$. Figures 4(a) and 4(b) show $|\Delta G_{\mathrm{AB}}|$ normalized to $M_1 M_2$, plotted as a function of M. With the decrease of M, the normalized amplitude $|\Delta G_{\mathrm{AB}}|/M_1 M_2$ exhibits fluctuations enveloped by an arc-shaped feature with a maximum at $M \sim 9$, demarcated by the dashed lines. Here, $|\Delta G_{\mathrm{AB}}|/M_1 M_2$ represents the AB amplitude contributed by one mode in each branch of the interferometer and is proportional to $\exp(-\tau\Gamma_\phi)$ [see Eq. (1)]. Hence, Figs. 4(a) and 4(b) reveal the M dependence of $\tau\Gamma_\phi$. To interpret our findings, we consider $\Gamma_\phi = \Gamma_{e-e} + \Gamma_{\mathrm{th}}$, where $\Gamma_{e-e} = (e/\hbar)^2 k_B T (C_\mu/C)^2 (R_{q1} + R_{q2})$ for parallel addable quantum wires [6,22] and $\Gamma_{\mathrm{th}} = k_B T/\hbar$ [9–12]. Here, C_μ is the electrochemical capacitance, C is the geometrical capacitance, and $R_{q1(2)}$ is the charge relaxation resistance of the upper (lower) wire. In our case, the interferometer remains charge neutral, so we can reasonably assume $C_\mu/C \sim 1$ [5,6]. Theoretically, the charge relaxation resistance of a ballistic wire varies with the density of states (DOS): $R_{q1(2)} = (h/8e^2)M_{1(2)}^{-1}$ when $G_{1(2)}$ is at a plateau position and the DOS of each channel is comparable, whereas

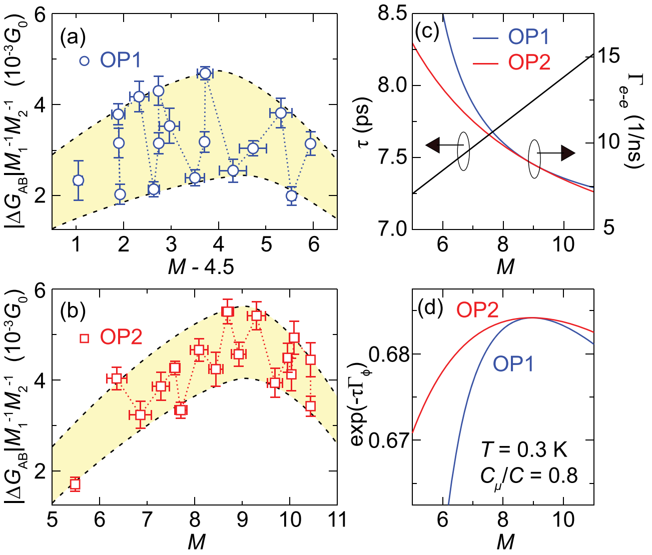

FIG. 4. The AB amplitude $|\Delta G_{\mathrm{AB}}|$ normalized to M_1M_2 as a function of M for (a) OP1 ($M = 4.5 + M_2$) and (b) OP2. The dashed lines are guides for the eyes, and denote the upper and lower bounds of the oscillatory features. (c) Calculation of τ and Γ_{e-e} for OP1 and OP2 as a function of M with $T = 0.3$ K and $C_\mu/C = 0.8$ (see the text). (d) The simulated factor $\exp(-\tau\Gamma_\phi)$ vs M.

$R_{q1(2)} = h/8e^2$ when $G_{1(2)}$ undergoes a mode transition and the DOS has a singularity at the threshold of a channel [15]. As a result, Γ_{e-e} oscillates with decreasing M. The oscillation of Γ_{e-e} qualitatively explains the observed fluctuations in $|\Delta G_{\mathrm{AB}}|/M_1M_2$. The fluctuations shown in Figs. 4(a) and 4(b) are reproducible; nevertheless, the dip minimums do not exactly match to the singularity positions of the DOS, predicted by the theory. This discrepancy may result from disorder effects, probably due to the mode mismatch at the junctions [14] or defects in the wires [23].

To understand the overall changes of $|\Delta G_{\mathrm{AB}}|/M_1M_2$, shown by the dashed lines, we shall consider the interplay of Γ_{e-e}, Γ_{th}, and τ with M. We provide a quantitative evaluation of the relevant parameters in the following. Figure 3(d) shows the $|\Delta G_{\mathrm{AB}}|$ vs T plot at $V_1 = V_2 = 0$ V. It appears that $|\Delta G_{\mathrm{AB}}| \propto \exp(-bT)$ with $b = 1.10 \pm 0.11\ \mathrm{K}^{-1}$, based on the best numerical fit. The value of b is comparable to the values in previous reports [3,8–12]. Note that $\tau\Gamma_\phi = bT$. We consider that the DOS for each mode is comparable, i.e., $R_{q1(2)} = (h/8e^2)M_{1(2)}^{-1}$, with $C_\mu/C = 0.8$ and obtain $\Gamma_{e-e}/\Gamma_{\mathrm{th}} \sim 0.2$ at $V_1 = V_2 = 0$ V. Figure 4(c) shows the calculated τ and Γ_{e-e} for OP1 and OP2 as a function of M with $T = 0.3$ K. Clearly, with depopulating M, τ decreases, and Γ_{e-e} increases while Γ_{th} is a constant of M, so that Γ_ϕ increases. Consequently, the factor $\exp(-\tau\Gamma_\phi)$ behaves as a concave function of M with a maximum at $M \sim 9$, which captures the essential trends observed in the experiments. In addition, the fact that we do not find any identifiable causal relation between δ_{ij} and $|\Delta G_{\mathrm{AB}}|/M_1M_2$ suggests that Γ_ϕ is uncorrelated to δ_{ij}, viz., the intermode scattering may have little effect on the dephasing processes.

By illustrating the mode dependence of Γ_ϕ, in essence, we demonstrate a route to link the phase coherence and the device geometry; namely, the coherence of a multimode quantum system, in principle, can be engineered. Taking a quantum interferometer as an example, we consider an annulus with a mean radius $r = \alpha M + r_0$, where r_0 is the inner radius and α is a geometric factor, which depends on the complementarity of the controlling gate, if any, and the wafer. The most optimized coherence per mode would be around $M = \sqrt{(\pi/4)(C_\mu/C)^2(r_0/\alpha)}$.

In conclusion, we studied the mode dependence of the phase coherence in a ballistic AB interferometer. We found that the AB amplitude is nearly proportional to M_1M_2 and fluctuates with the reduction of M, and the normalized AB amplitude shows a maximum at $M \sim 9$. The observed M dependences of the AB amplitude can be explained by recent theories based on the charge-fluctuation-induced dephasing process. The phase coherence in a multimode quantum wire is governed by the interplay of the geometric effects, the thermal averaging effect, and the e-e interaction induced decoherence. We verify that the singularity of DOS in a quasi-1D wire plays an important role in decoherence and clarify that the intermode scattering is not the dominant dephasing source. Our findings have important implications for the decoherence mechanisms and for the design of future quantum electronic devices.

We acknowledge the late Markus Büttiker for valuable discussions and Pei-Jung Wu for experimental assistance. This project is supported by Ministry of Science and Technology under Grant No. NSC 101-2628-M-007-002-MY3, Taiwan.

---

[*] Corresponding author.
jcchen@phys.nthu.edu.tw

[1] Y. Imry, *Introduction to Mesoscopic Physics*, ed. 2 (Oxford University Press, New York, 2002).
[2] M. Schlosshauer, Rev. Mod. Phys. **76**, 1267 (2005).
[3] M. Yamamoto, S. Takada, C. Bauerle, K. Watanabe, A. D. Wieck, and S. Tarucha, Nat. Nanotechnol. **7**, 247 (2012).
[4] M. Casse, Z. D. Kvon, G. M. Gusev, E. B. Olshanetskii, L. V. Litvin, A. V. Plotnikov, D. K. Maude, and J. C. Portal, Phys. Rev. B **62**, 2624 (2000).
[5] G. Seelig and M. Büttiker, Phys. Rev. B **64**, 245313 (2001).
[6] M. Büttiker, in *Quantum Mesoscopic Phenomena and Mesoscopic Devices in Microelectronics*, NATO Science Series, edited by I. Kulik and R. Ellialtioğlu (Springer, Netherlands, 2000), Vol. 559, p. 211.
[7] C. Texier, P. Delplace, and G. Montambaux, Phys. Rev. B **80**, 205413 (2009).
[8] A. E. Hansen, A. Kristensen, S. Pedersen, C. B. Sørensen, and P. E. Lindelof, Phys. Rev. B **64**, 045327 (2001).

[9] K. Kobayashi, H. Aikawa, S. Katsumoto, and Y. Iye, J. Phys. Soc. Jpn. **71**, 2094 (2002).
[10] Y. Yamauchi, M. Hashisaka, S. Nakamura, K. Chida, S. Kasai, T. Ono, R. Leturcq, K. Ensslin, D. C. Driscoll, A. C. Gossard, and K. Kobayashi, Phys. Rev. B **79**, 161306 (2009).
[11] K.-T. Lin, Y. Lin, C. C. Chi, J. C. Chen, T. Ueda, and S. Komiyama, Phys. Rev. B **81**, 035312 (2010).
[12] S. S. Buchholz, S. F. Fischer, U. Kunze, M. Bell, D. Reuter, and A. D. Wieck, Phys. Rev. B **82**, 045432 (2010).
[13] C. W. J. Beenakker and H. van Houten, Solid State Phys. **44**, 1 (1991).
[14] E. Castano and G. Kirczenow, Phys. Rev. B **41**, 5055 (1990).
[15] M. Büttiker, J. Korean Phys. Soc. **34**, 121 (1999).
[16] M. Macucci and K. Hess, Phys. Rev. B **46**, 15357 (1992).
[17] See Supplemental Material at http://link.aps.org/supplemental/10.1103/PhysRevLett.116.080401 for the full voltage range conductance map.
[18] R. C. Villarreal, F. Mireles, E. E. Marinero, and B. A. Gurney, Appl. Phys. Lett. **98**, 172102 (2011).
[19] T.-S. Lo, Y. Lin, and J.-C. Chen, Phys. Rev. B **85**, 245416 (2012).
[20] M. Buttiker, Y. Imry, R. Landauer, and S. Pinhas, Phys. Rev. B **31**, 6207 (1985).
[21] G. Cernicchiaro, T. Martin, K. Hasselbach, D. Mailly, and A. Benoit, Phys. Rev. Lett. **79**, 273 (1997).
[22] G. Iannaccone, M. Macucci, and B. Pellegrini, Phys. Rev. B **56**, 12104 (1997).
[23] P. F. Bagwell, Phys. Rev. B **41**, 10354 (1990).